Nano Energy 151 (2026) 111859

Contents lists available at ScienceDirect

Nano Energy

journal homepage: www.elsevier.com/locate/nanoen

Full paper

Circularly polarized electroluminescence from thermally evaporated core-shell perovskite-based light-emitting diodes

Min Hyeong Lee [a,1], Yong-Jun Choi [b,1], Jongbeom Kim [b], Jungho Han [b], Jinkyu Yang [b], Donghan Kim [b], Dongeun Kim [a], Juyoung Kim [b], Han Gi Chae [b], Young Chul Jun [b], Myoung Hoon Song [a,b,*]

[a] Graduate School of Semiconductor Materials and Devices Engineering, Center for Future Semiconductor Technology (FUST), Ulsan National Institute of Science and Technology (UNIST), Ulsan 44919, Republic of Korea
[b] Department of Materials Science and Engineering, Ulsan National Institute of Science and Technology (UNIST), Ulsan 44919, Republic of Korea

ARTICLE INFO

Keywords:
Thermal evaporation
Circular polarization
Perovskite light-emitting diodes
Core-shell structure
Circularly polarized electroluminescence

ABSTRACT

Spin light-emitting diodes (spin-LEDs) have garnered significant attention for their potential applications in quantum information technology, three-dimensional displays, and secure optical communications. Although solution-processed spin-LEDs have advanced rapidly, they exhibit limited scalability and reproducibility. By contrast, spin-LEDs fabricated via thermal evaporation offer scalability and reproducibility but remain underdeveloped owing to uncontrolled crystallization and significant nonradiative recombination. In this study, we developed efficient perovskite spin-LEDs via multisource sequential evaporation utilizing $PbBr_2$, chiral [1,1′-binaphthalene]-2,2′-diylbis[1,1-diphenyl-1,1′-phosphineoxide] (BINAPO) molecules, and CsBr. The chiral BINAPO molecules with bidentate $(P=O)_2$ groups surround the $CsPbBr_3$ lattice to form a perovskite–BINAPO structure. This structure controls perovskite crystallization, passivates surface defects, and enhances the exciton binding energy. Furthermore, the chiral-induced spin-selectivity effect of the chiral BINAPO shell alters the spin states of the injected carriers, which are subsequently transferred to the perovskite core, leading to the emergence of chiro-optical properties in the perovskite. The resulting perovskite spin-LEDs achieve maximum external quantum efficiencies of 13.20% (R-target) and 12.35% (S-target), in conjunction with electroluminescence dissymmetry factors of −0.124 (R-target) and 0.106 (S-target). This study presents the first demonstration of circularly polarized electroluminescence from thermally evaporated perovskite spin-LEDs, building a scalable platform for high-efficiency spin optoelectronics and practical perovskite spin-LEDs integration.

1. Introduction

In the past decade, halide perovskites have emerged as promising materials for next-generation displays owing to their exceptional optoelectronic properties [1–4]. Perovskite spin light-emitting diodes (spin-LEDs) have attracted considerable attention for applications in quantum information technology, three-dimensional (3D) displays, and secure optical communication [5–8]. To exploit the spin-related properties of perovskite light-emitting diodes (PeLEDs), chiral groups act as spin filters to generate an asymmetric population of spin-polarized carriers in the perovskite layer via the chiral-induced spin selectivity (CISS) effect [9–12].

The solution-processed perovskite spin-LEDs can be categorized into several structural configurations [13–21]. Chiral two-dimensional (2D) perovskites serve as spin-selective layers via the CISS effect, wherein the R- or S-configuration induces spin-up or spin-down polarization of injected carriers, resulting in left- and right-handed circularly polarized light (CPL) emissions from the emissive layer, corresponding to the R- or S-configuration (L-CPL and R-CPL, respectively). In some chiral perovskite systems, spin polarization originates from organic-to-inorganic structural chirality transfer, in which chiral organic components induce lattice distortion in the inorganic perovskite framework, enabling spin-polarized emission upon photon absorption in the inorganic domain [22–24]. perovskite spin-LEDs incorporating chiral 2D

* Corresponding author at: Graduate School of Semiconductor Materials and Devices Engineering, Center for Future Semiconductor Technology (FUST), Ulsan National Institute of Science and Technology (UNIST), Ulsan 44919, Republic of Korea.
E-mail address: mhsong@unist.ac.kr (M.H. Song).
[1] These authors contributed equally to this work

https://doi.org/10.1016/j.nanoen.2026.111859
Received 12 January 2026; Received in revised form 23 February 2026; Accepted 5 March 2026
Available online 6 March 2026
2211-2855/© 2026 Elsevier Ltd. All rights are reserved, including those for text and data mining, AI training, and similar technologies.

perovskite interlayers exhibit a high degree of spin polarization [25]. However, these devices suffer from low efficiency owing to poor charge carrier transport attributed to the large bandgap and spin relaxation at the interface. [19] Consequently, both the external quantum efficiency (EQE) and dissymmetry factor remain limited. By contrast, chiral quasi-2D perovskites generate spin-polarized carriers in the chiral 2D perovskites, whose spin and energy are funneled into 3D perovskites that act directly as CPL-emissive layers, thereby facilitating CPL emission. [16] Nevertheless, the population of spin-polarized carriers may decrease owing to spin relaxation, further reducing the degree of spin polarization in conjunction with the inherent stability limitations of chiral quasi-2D perovskites [26]. Recently, structural strategies such as the incorporation of chiral ligands and core–shell architectures have been employed in perovskite spin-LEDs to achieve high electroluminescence (EL) dissymmetry factors ($g_{CP\text{-}EL}$) and efficient light emission because spin-polarized excitons generated via the CISS effect rapidly recombine and emit CPL owing to their large exciton binding energy [18–21]. To address the limitation of short spin lifetimes in carriers injected via the CISS effect at room temperature, perovskite spin-LEDs must be designed to enable rapid recombination, which is crucial for effective CPL emission [27].

Currently, highly efficient CP-PeLEDs are predominantly fabricated employing solution-based methods, which encounter scalability and reproducibility issues, as well as compatibility issues with commercial organic LED (OLED) facilities. In addition, solvent-related costs and incompatibility with OLED facilities further increase the manufacturing costs, making solution processes unsuitable for practical applications. To address these challenges, thermal evaporation offers a promising alternative as it eliminates the need for solvents, ensures compatibility with the OLED manufacturing infrastructure, and provides excellent scalability and process uniformity [28]. However, systematic studies on thermal evaporation for production of perovskite spin-LEDs have not yet been reported, highlighting a significant gap in the current literature. Thermally evaporated PeLEDs often exhibit inferior performance compared with solution-processed PeLEDs, primarily because of uncontrolled crystal growth that generates undesirable defect sites, which in turn promote trap-assisted non-radiative recombination [28–30]. To address this issue, electron-donating additives that coordinate with PbX_2 during thermal evaporation have been shown to control the crystallization and passivate defect sites, resulting in EQEs exceeding 16% and demonstrating the strong potential of thermally evaporated PeLEDs [29,30]. Notably, to realize successful thermally evaporated perovskite spin-LEDs, such strategies must also be compatible with the spin-related properties that are critical for circularly polarized light emission.

In this study, we fabricated thermally evaporated perovskite spin-LEDs incorporating a well-defined perovskite–chiral [1,1′-binaphthalene]-2,2′-diylbis[1,1-diphenyl-1,1′-phosphineoxide] (BINAPO) core–shell structure. The formation of a versatile chiral BINAPO shell controls perovskite crystallization, resulting in a significantly reduced grain size in the perovskite film. The core–shell structure induces strong carrier and dielectric confinement at the organic–inorganic interface, thereby enhancing the exciton binding energy. Furthermore, the bidentate $(P=O)_2$ groups of the BINAPO shell effectively coordinate with undercoordinated Pb^{2+} ions, suppressing trap-assisted non-radiative recombination, thereby improving optoelectronic properties. In terms of chiro-optical functionality, the BINAPO shell acts as a CISS active layer that modifies the spin states of the injected carriers, which are subsequently transferred to the perovskite core to efficiently recombine and form spin excitons that generate circularly polarized EL (CP-EL). This recombination is further facilitated by the large exciton binding energy resulting from the strong exciton and dielectric confinement in the core–shell structure. Consequently, the thermally evaporated perovskite spin-LEDs based on the $CsPbBr_3$–BINAPO core–shell structure reached maximum EQEs of 13.20% (R-target) and 12.35% (S-target), in conjunction with $g_{CP\text{-}EL}$ of −0.124 (R-target) and 0.106 (S-target). Our study represents the first demonstration of CP-EL from thermally evaporated perovskite spin-LEDs, establishing a scalable platform for high-efficiency spin optoelectronics.

2. Experimental section

2.1. Materials

Glass/ITO (12 Ω sq−1, AMG), CsBr (ultra-dry, 99.999%, metal basis, Alfa Aesar), $PbBr_2$ (ultra-dry, 99.998%, metal basis, Alfa Aesar), 2-[4-(9,10-Di-naphthalen-2-yl-anthracen-2-yl)-phenyl]-1-phenyl-1H-benzoimidazole(ZADN) (Ossila), (R)-[1,1′-Binaphthalene]-2,2′-diylbis[1,1-diphenyl-1,1′-phosphineoxide](99%, AmBeed), (S)-[1,1′-Binaphthalene]-2,2′-diylbis[1,1-diphenyl-1,1′-phosphineoxide] (99%, AmBeed), LiF (99.9%, TASCO), Al (99.99%, 3 mm pellets, TASCO), PEDOT:PSS (AI 4083, Clevios), ethanolamine (Sigma-Aldrich), DMSO-d6 (99.9 atom % D, sigma Aldrich) and NafionTM perfluorinated resin solution (Aladdin) were used as-received, without further purification.

2.2. Device fabrication

Glass/ITO electrode substrates were cleaned through sonication for 30 min in sequence using deionized water, acetone, and isopropyl alcohol, followed by exposure to UV ozone for an additional 30 min. The HTL was prepared by mixing PEDOT:PSS, NafionTM perfluorinated resin solution, and ethanolamine in a volume ratio of 2:1:0.05. The mixture was stirred for 24 h before use. The HTL solution was spin-coated onto the pre-patterned ITO substrate at 2000 rpm (second step) for 43 s and annealed at 150 °C for 20 min. The substrates were loaded into a high vacuum chamber to evaporate the perovskite layer. $PbBr_2$, R-/S- BINAPO, and CsBr were thermally evaporated at rates below 0.5, 0.1, and 0.9 Å/s, respectively. For layer-by-layer sequential thermal evaporation, 9 pairs of $PbBr_2$, R-/S- BINAPO, and CsBr were deposited, with thicknesses of 1.5 nm for $PbBr_2$, 2.5 nm for R-/S- BINAPO, and 2.5 nm for CsBr. After evaporation, the perovskite films were transferred into a N_2-filled glovebox and annealed at 110 °C for 20 min. After cooling, 30-nm-thick ZADN, 1-nm-thick LiF, and 100-nm-thick Al layers were continuously thermally evaporated under a high vacuum of 3×10^{-6} Torr.

2.3. Characterization of perovskite film

SEM was performed using a Nova NanoSEM 230 (Hillsboro, OR, USA) instrument operated at 10 kV. UV-Vis spectroscopy was conducted by Cary 5000, Agilent Technology. The PLQY was performed using a Quantaurus-QY Plus UV-NIR absolute PL quantum yield spectrometer (C13534–33, Hamamatsu Corp.) equipped with a Xenon lamp as a light source and a 3.3 in. integrating sphere, the excitation wavelength was 400 nm. Two-dimensional grazing incidence X-ray diffraction measurements were obtained at the Pohang Accelerator Laboratory (PAL, Korea, beamline PLS-II 6D). A two-dimensional charge-coupled device detector (pixel size of 0.078 nm, MX225-HS, Rayonix L.L.C.), placed at a distance of 240.4 mm from the samples, was used to record the scattering patterns. The incident angle was fixed at 0.11°. XPS investigations were performed using a K-Alpha spectrometer (Thermofisher Scientific, Waltham, MA, USA) with Al Kα nonmonochromatic X-ray excitation. Time-resolved photoluminescence spectra were obtained using a time-correlated single-photon counting setup (FluoTime 300, PicoQuant, Germany). ^{207}Pb NMR was measured with 600 MHz AVANCE NEO 600 (Bruker). Temperature-dependent conductivity was measured using a cryogenic probe station (Lakeshore CRX-4K) with a Keithley 4200-SCS detector at 10–300 K. UPS analysis was conducted using a UPS system (AXIS Nova, Kratos Analytical) with a He (21.2 eV) ultraviolet source. Absorption and CD spectra was carried out using CD spectrometer (Jasco CD J-1700, Jasco Inc.) at the KAIST Analysis Center for Research Advancement (KARA). CPPL measurement was carried out using CPL spectrophotometer (Jasco CPL-300, Jasco Inc.) at the KAIST Analysis

Center for Research Advancement (KARA). The CPEL measurement is set up as shown in Fig. S20, the emitted light passes through a quarter-wave plate, converting it into linearly polarized light, and then passes through a linear polarizer, after which the intensity is compared. The left and right CPL signals were separated by rotating the linear polarizer by 90°. Prior to the magnetic conductive probe AFM measurement, the Co–Cr-coated AFM tips were magnetized using a permanent magnet for 30 min. A resonance frequency of 75 kHz was applied during the mc-AFM measurements. The I–V characteristics were repeatedly measured at room temperature under a sweeping bias from –4 V to + 4 V. The device structure used for spin-polarized current measurements was ITO/HTL/perovskite/Co–Cr tip. The performance of encapsulated PeLEDs were measured using a Keithley 2400 source meter and spectroradiometer (CS-2000, Konica Minolta) under ambient conditions.

3. Results and discussion

Perovskite thin films were fabricated via multi-source sequential evaporation of $PbBr_2$, BINAPO, and CsBr (Fig. 1a, Fig. S1). Given the susceptibility of organic molecules to decomposition during thermal evaporation, the thermal stability of BINAPO was investigated. Thermogravimetric analysis revealed negligible weight loss below 270 °C, indicating robustness during evaporation, whereas BINAPO began to evaporate at approximately 150 °C during the thermal evaporation process (Fig. S2). The perovskite morphology obtained by incorporating BINAPO during thermal evaporation was analyzed. Scanning electron microscopy (SEM) measurements revealed significant differences between the control and target perovskite films. The control films exhibited large grains, indicating uncontrolled crystallization and grain coarsening (Fig. 1b). By contrast, the target perovskite film exhibited a

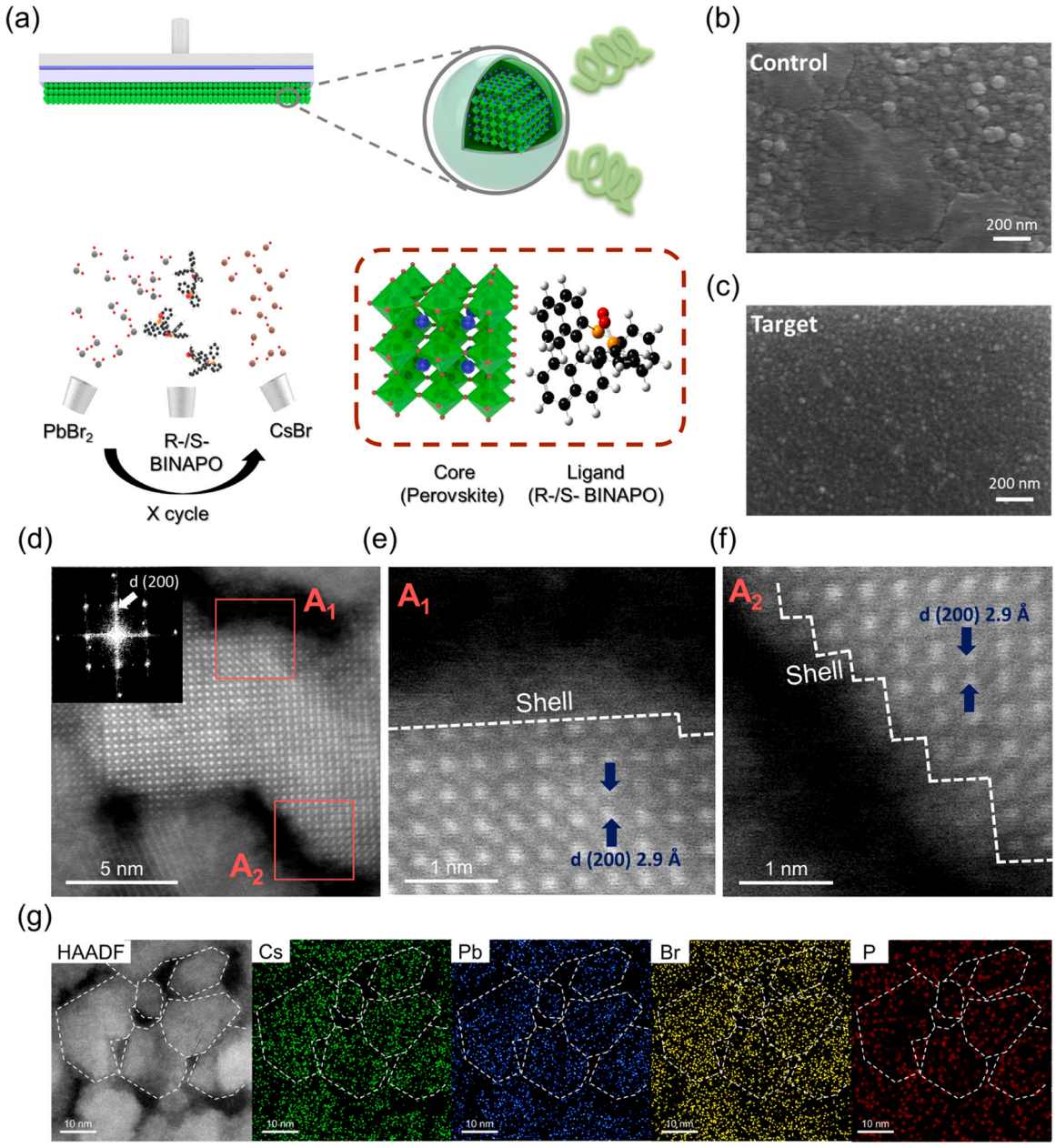

Fig. 1. Formation of a $CsPbBr_3$/BINAPO core/shell structure via multi-source sequential evaporation. (a) Schematic of multi-source sequential evaporation of $PbBr_2$, BINAPO, and CsBr. SEM images of the (b) control and (c) target perovskite films. (d) HAADF-STEM image of the target perovskite film (inset: fast Fourier transform (FFT) patterns of the $CsPbBr_3$ cubic lattice). Magnified views of HAADF-STEM images of the surface areas of the target perovskite film. (e) A_1 and (f) A_2. (g) HAADF-STEM and EDS mappings of the target perovskite film showing the distribution of Cs (green), Pb (blue), Br (orange), and P (red) on the grains.

more uniform morphology with substantially smaller grains, demonstrating that the incorporation of BINAPO effectively controlled the crystal growth and formed a homogeneous microstructure (Fig. 1c). The microstructural changes caused by the addition of BINAPO were observed via high-angle annular dark-field scanning transmission electron microscopy (HAADF-STEM). The control perovskite film exhibits relatively large grains, whereas the BINAPO-incorporated target perovskite film shows significantly reduced grain sizes on the order of ~20 nm scale. During crystallization, BINAPO molecules attach to the perovskite surface, forming a shell that facilitates the formation of a core–shell structure. HAADF-STEM imaging confirmed the presence of a 3D $CsPbBr_3$ lattice with a lattice spacing of 0.29 nm corresponding to the (200) plane of the core and showed a well-defined interface between the perovskite core and the surrounding BINAPO shell. However, in the control film, the HADDF-STEM image shows that the crystalline perovskite region is clearly distinguished from the surrounding dark contrast region, and the lattice pattern extend uniformly to the grain surface (Fig. 1d, e, f, Fig. S3, and S4) [31], [32]. Energy-dispersive X-ray spectroscopy (EDS) mapping shows the core-shell structure (Fig. 1g and Fig. S4). The Cs, Pb, and Br signals were confined within the perovskite grains, verifying the composition of the $CsPbBr_3$ lattice. The P signal associated with BINAPO was observed throughout the film, with a tendency to appear near the grain regions, consistent with its role in forming a shell-like interfacial environment around the perovskite grains.

To investigate the structural changes between the control and target perovskite films, we conducted grazing-incidence wide-angle X-ray scattering (GIWAXS) measurements (Fig. S5). The 2D GIWAXS patterns

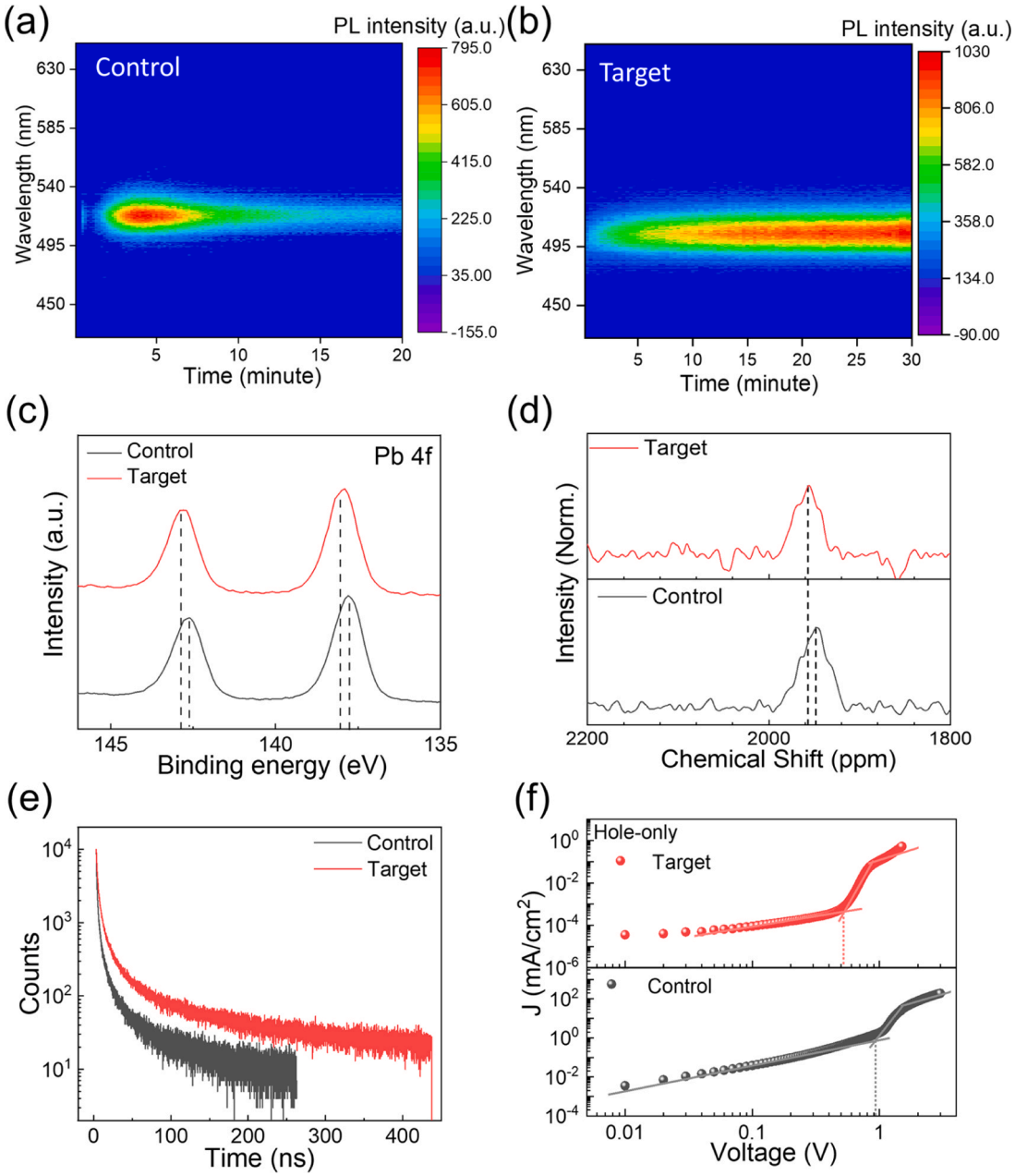

Fig. 2. Interaction between BINAPO and perovskite during crystallization. In situ photoluminescence (PL) spectra of (a) the control and (b) target perovskite film during annealing. (c) XPS spectra of the Pb 4 f signal in the control and target perovskite films. (d) ^{207}Pb NMR measurement of the control ($PbBr_2$ only) and target perovskite (a mixture of $PbBr_2$ and BINAPO) dispersed in DMSO-d6. (e) Time-correlated single-photon counting (TCSPC) data of the control and target perovskite films. (f) Space-charge-limited current (SCLC) analysis of the hole-only devices with the control and target perovskite films. In this figure, R-BINAPO was used for preparing target perovskite films.

of the control and target perovskite films exhibited three primary peaks corresponding to the (100), (110), and (200) planes of the $CsPbBr_3$ structure. Compared with the control film, the three primary peaks of the target perovskite film exhibited wider full widths at half maximum, confirming reduced grain sized. Furthermore, we measured the UV–visible absorption spectra and employed ultraviolet photoelectron spectroscopy (UPS) to investigate the optical bandgaps and energy levels of the control and target perovskite films and BINAPO molecules (Fig. S6 and S7). The control film exhibited two absorption peaks at 511 and 315 nm, corresponding to the 3D phase ($CsPbBr_3$) and zero-dimensional (0D) phase (Cs_4PbBr_6), respectively. The 315 nm peak attributed to the 0D phase was suppressed in the target perovskite film, likely owing to steric hindrance of the chiral BINAPO molecules [30]. By contrast, the target perovskite film exhibited two absorption peaks at 500 and 335 nm, corresponding to the 3D phase ($CsPbBr_3$) and the characteristic absorption of BINAPO, respectively. The blue shift of the 3D phase ($CsPbBr_3$) peak from 511 to 500 nm was attributed to the grain size reduction induced by BINAPO. The presence of the 335-nm peak, also observed in the absorption spectrum of the BINAPO molecule, confirming its molecular origin.

Tauc plot analysis of the films revealed optical bandgaps of 2.37 eV for the control film, 2.41 eV for the target perovskite film, and 3.62 eV for BINAPO (Fig. S8). The wider-bandgap BINAPO (3.62 eV) surrounding the 3D $CsPbBr_3$ (2.41 eV) leads to carrier and dielectric confinement at the organic–inorganic interface, strengthening excitonic effects in the target perovskite film [33–35]. This confinement effect significantly increased the exciton binding energy from 84.91 to 261.31 meV as grain size reduced, as confirmed by temperature-dependent photoluminescence (PL) measurements (Fig. S9 and **Supplementary Note 1**).

The crystallization kinetics of the control and target perovskite films were investigated by performing in-situ PL measurements during thermal annealing. The experimental setup is shown in Fig. S10. A 365-nm UV light source was used for excitation, placed within a nitrogen-filled glovebox to minimize moisture and oxygen exposure, and the emitted PL signal was collected via an optical fiber. As shown in Fig. 2a, the PL intensity of the control film remained nearly constant for the next 6 min. Subsequently, the PL intensity decreased rapidly owing to uncontrolled crystallization during annealing. By contrast, the PL emission of the target perovskite film increased significantly for over 30 min, suggesting that the addition of the chiral BINAPO molecule effectively controlled the crystallization process, leading to a reduced grain size in the perovskite during annealing (Fig. 2b).

The role of the chiral BINAPO molecules in modulating crystallization was further investigated employing electrostatic potential (ESP) mapping, X-ray photoelectron spectroscopy (XPS), and nuclear magnetic resonance (NMR) analyses. As shown in Fig. S11, BINAPO adopts a bidentate structure (i.e., $(P=O)_2$) with regions of negative ESP (red) localized around the oxygen atoms of the two phosphine oxide groups, indicating high electron density [36−39]. XPS analysis revealed that the Pb 4 f peak of the target perovskite film shifted to a higher binding energy than that of the control, which was attributed to the replacement of Br^- with more electronegative oxygen atoms via chemical interactions between the P = O groups and Pb^{2+} ions (Fig. 2c) [30,40]. Reflecting this interaction, a corresponding shift was observed in the Br 3d peak; however, no shift was detected in the Cs 3d peak (Fig. S12). In addition, ^{207}Pb NMR spectra of the control ($PbBr_2$) and target perovskite ($PbBr_2$–BINAPO mixture) films showed a distinct chemical shift, confirming the coordination between BINAPO and Pb and indicating a modified local chemical environment (Fig. 2d). Collectively, these results demonstrate that BINAPO acts as a bidentate ligand that coordinates with Pb^{2+} ions and regulates crystal growth, thereby reducing grain size during perovskite crystallization.

In addition to grain size reduction during crystallization, the chiral BINAPO was introduced to simultaneously enhance the optoelectronic and chiro-optical properties of the perovskites, both of which are essential for achieving high-performance perovskite spin-LEDs. To comprehensively analyze the role of the chiral BINAPO in enhancing the optoelectronic properties, we performed time-correlated single-photon counting (TCSPC) measurements. According to the TCSPC results, the target perovskite film exhibited a longer average PL decay lifetime (8.48 ns) compared with those of the control film (3.36 ns) (Fig. 2e and Table S1). Under the same measurement conditions, the target perovskite film exhibited a significantly higher PL intensity than that of the control film. Additionally, the target perovskite film exhibited PL quantum yield of 58.5%, which was significantly higher than that of the control film (12.2%) (Fig. S13). This enhancement is attributed to the introduction of chiral BINAPO, which increases the exciton binding energy and effectively suppresses trap-assisted nonradiative recombination by defect passivation. To further analyze the optoelectronic properties, dark J–V measurements of hole-only devices (ITO/m-PEDOT:PSS/perovskites/MoO_3/Ag) were conducted to compare the trap densities of the control and target perovskite films employing space-charge-limited current (SCLC) analysis (Fig. 2f and **Supplementary Note 2**). The control device exhibited a trap-filling limit voltage (V_{TFL}) of 0.84 V, corresponding to a trap density (n_{trap}) of 1.72×10^{20} cm^{-3}, whereas the target perovskite device exhibited a lower V_{TFL} of 0.54 V, and a reduced n_{trap} of 1.07×10^{20} cm^{-3}. The reductions in V_{TFL} and n_{trap} are attributed to effective defect passivation by the chiral BINAPO, which is consistent with the enhanced PL intensity, prolonged PL lifetime, and increased PL quantum yield observed for the target perovskite film.

Circular dichroism (CD) spectroscopy was performed to investigate the chiro-optical properties of the R-/S-target perovskite films. In this study, the differential absorption spectra of left- and right-handed CPL ($\Delta\varepsilon = \varepsilon_L - \varepsilon_R$) were recorded in the spectral range of 200–600 nm. The CD spectra of the R-/S-target perovskite films exhibited distinct absorption bands within this range (Fig. 3a, b, and Fig. S14). Accordingly, the R-/S-BINAPO films exhibited mirror-image CD signals in the corresponding absorption region, in conjunction with a distinct Cotton effect (Fig. S15). The highest-energy absorption band observed near 235 nm originates from the $\pi \rightarrow \pi^*$ transition of the naphthyl groups in chiral BINAPO [36,41]. As shown in Fig. S16, the $\pi \rightarrow \pi^*$ satellite group is observed at approximately 291 eV in the XPS C 1 s spectra of both R-/S-target perovskite and R-/S-BINAPO films, confirming the presence of the $\pi \rightarrow \pi^*$ transition. In addition, the lower-energy absorption bands at approximately 300 nm and near 335 nm were attributed to the $n \rightarrow \pi^*$ transition from the P = O group to the naphthyls, and the characteristic absorption of the chiral BINAPO, respectively. Both absorption bands exhibited Cotton effects with mirror-image signals depending on the handedness of BINAPO (R- or S-). To minimize the effects of linear birefringence and dichroism in the target perovskite films, the samples were rotated and flipped within the observation plane (normal to the direction of incident light) during the measurements [42], [43]. After rotating the sample by 90°, flipping it, and subsequently rotating it again by 90°, no prominent change in the CD signal was observed, indicating that the signal did not originate from the anisotropy of the perovskite crystal (Fig. S17). Additionally, circularly polarized photoluminescence (CPPL) measurements were conducted, revealing mirror-image signals that can be attributed to chiral core–shell perovskites (Fig. 3**c**). Furthermore, control experiments using racemic BINAPO were performed to verify the origin of the chiro-optical properties. No detectable CD or CPL signals were observed in the racemic sample, confirming that the observed circular polarization originates from the molecular chirality of BINAPO (Fig. S18). These results demonstrate that the incorporation of chiral R-/S-BINAPO induces chiro-optical activity in perovskite films.

To validate the spin-selectivity effect of the chiral core–shell perovskites induced by mirror-symmetric distortion of the R-/S-BINAPO shells via the CISS effect, magnetic conductive-probe atomic force microscopy (mCP-AFM) measurements were performed [44]. The conductive AFM tip was coated with Co/Cr and magnetized to selectively inject spin-polarized carriers (spin-up or spin-down) (Fig. 3d). The device

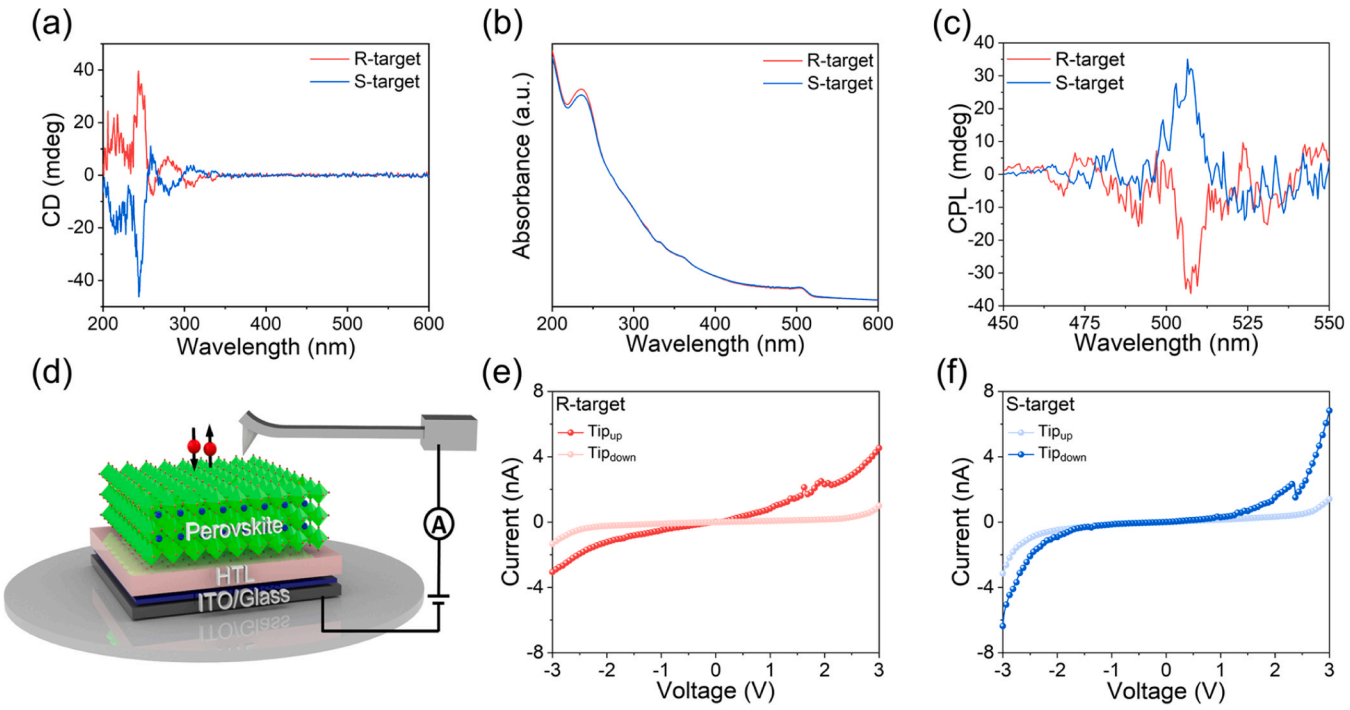

Fig. 3. Chiro-optical characterizations of chiral perovskite. (a) CD spectra of the R- and S-target perovskite films. (b) UV–vis absorption spectra of the R- and S-target perovskite films. (c) Circularly polarized photoluminescence (CPPL) spectra of the R- and S-target perovskite films. (d) Schematic illustration of mCP-AFM analysis. *I-V* curves under different injected spin polarizations based on the (e) R- and (f) S-target perovskite films.

structure comprises ITO/m-PEDOT:PSS/chiral perovskites. To evaluate the spin-dependent charge transport, the spin polarization (P) was calculated using the relation $P = (I_{up} - I_{down})/(I_{up} + I_{down})$, where I_{up} and I_{down} correspond to the measured currents in the up and down magnetization states [45]. The average current–voltage (I–V) curves were measured (Fig. S19), and the P values of the R- and S-target perovskite films at 3 V were 63.9% and −65.7%, respectively (Fig. 3e and f). These findings indicate that the handedness of BINAPO induces mirror-symmetric distortions in the shell, which in turn lead to spin selectivity in the chiral core–shell perovskites via the CISS effect.

Leveraging the synergistic enhancement of both optoelectronic and chiro-optical properties in the perovskite film, we fabricated perovskite spin-LEDs with glass/ITO/m-PEDOT:PSS/chiral perovskites/ 2-[4-(9,10-Di-naphthalen-2-yl-anthracen-2-yl)-phenyl]-1-phenyl-1H-benzoimidazole(ZADN)/LiF/Al using control and target perovskite devices incorporating R-/S-BINAPO (denoted as R-target and S-target, respectively) (Fig. 4a and Table S2). The energy levels of the control and R-/S-target perovskite layers, as determined by UPS and UV–vis spectra, are presented in Fig. S20. Fig. 4b, c, and d show the current density–voltage–luminance (J–V–L) characteristics, EQE–current density (EQE–J) curves, and EQE distributions for the control, R-, and S-target perovskite devices. Both the R- and S-target perovskite devices exhibited a turn-on voltage (V_T) of 2.0 V, and maximum luminance values of 9747.5 cd/m^2 and 10,692 cd/m^2, respectively. In particular, the R- and S-target perovskite devices achieved maximum EQE values of 13.20% and 12.35%, respectively, approximately a six-fold enhancement over that of the control device (~2.4%). This improvement can be attributed to the enhanced optoelectronic properties of the R-/S-target perovskite layers owing to the significantly reduced grain size and defect passivation induced by the chiral BINAPO molecule. Furthermore, the EQE distributions obtained from the 15 control and R-/S-target perovskite devices exhibited high reproducibility (Fig. 4d). Fig. 4e shows the EL spectra of the control and R-/S-target perovskite devices. The EL peak initially observed at 518 nm in the control devices shifted to 510 nm in the R-/S-target perovskite devices. This EL shift aligns with the temperature-dependent PL analysis and can be attributed to the strong confinement effect induced by the reduced grain size.

The operational stability of the perovskite spin-LEDs was measured under constant-current conditions using the R-target perovskite devices. For the R-target perovskite devices, the T_{50} values were 163.95, 157.55, 68.85, 63.58, 45.03, 52.93, 41.63, and 44.33 min at initial luminance values of 889.5, 1357.7, 2538.9, 2611.2, 3535.4, 3643.3, 4056.1, and 4432.7 cd/m^2, respectively (Fig. S21). The accelerated lifetime equation ($L_0^n T_{50}$ = constant, where n is the acceleration factor, set to 1.03 in this study) was introduced to extrapolate the operational stability under standard luminance conditions. The T_{50} value of the R-target perovskite device at 100 cd/m^2 was calculated to be 30.56 h (Fig. 4f).

To investigate the efficiency of CP-EL from perovskite spin-LEDs, we evaluated the R-/S-target perovskite devices by comparing the intensities of the L-CPL and R-CPL emissions utilizing a custom-built Fourier-plane measurement setup (Fig. S22) [46]. The CP-EL was measured at 2.8 V, the integration time was set to 5 s. The $g_{CP\text{-}EL}$ values for the CP-EL measurements were calculated as described in **Supplementary Note 3**. The target perovskite devices incorporating 1.5 nm-thick R-/S-BINAPO layers per deposition cycle exhibited negligible intensity differences between the left- and right-handed CP-EL (L-CP-EL and R-CP-EL), corresponding to relatively low $g_{CP\text{-}EL}$ values of −0.0062 and 0.0024 for the R- and S-target perovskite devices, respectively (Fig. S23). Insufficient amounts of chiral R-/S-BINAPO reduced the CISS effect, resulting in inferior chiro-optical properties. By contrast, the target perovskite devices with an optimized chiral R-/S-BINAPO layer (2.5 nm-thick R-/S-BINAPO layers per deposition cycle) exhibited a distinct intensity difference between R-CP-EL and L-CP-EL (Fig. 4**g**). The handedness of the emitted CP-EL signals aligned with the chirality of R- or S-BINAPO, indicating efficient spin manipulation. For comparison, a control device fabricated using racemic BINAPO was also measured under identical conditions. In this case, only a negligibly small CP-EL signal was observed, with a $g_{CP\text{-}EL}$ value significantly lower than those of the R- and S-devices, indicating the absence of meaningful circular polarization (Fig. S24). Accordingly, the spin states of the injected carriers were altered by the CISS effect of the chiral BINAPO shell, and the spin-polarized carriers were transferred to the $CsPbBr_3$ core and rapidly

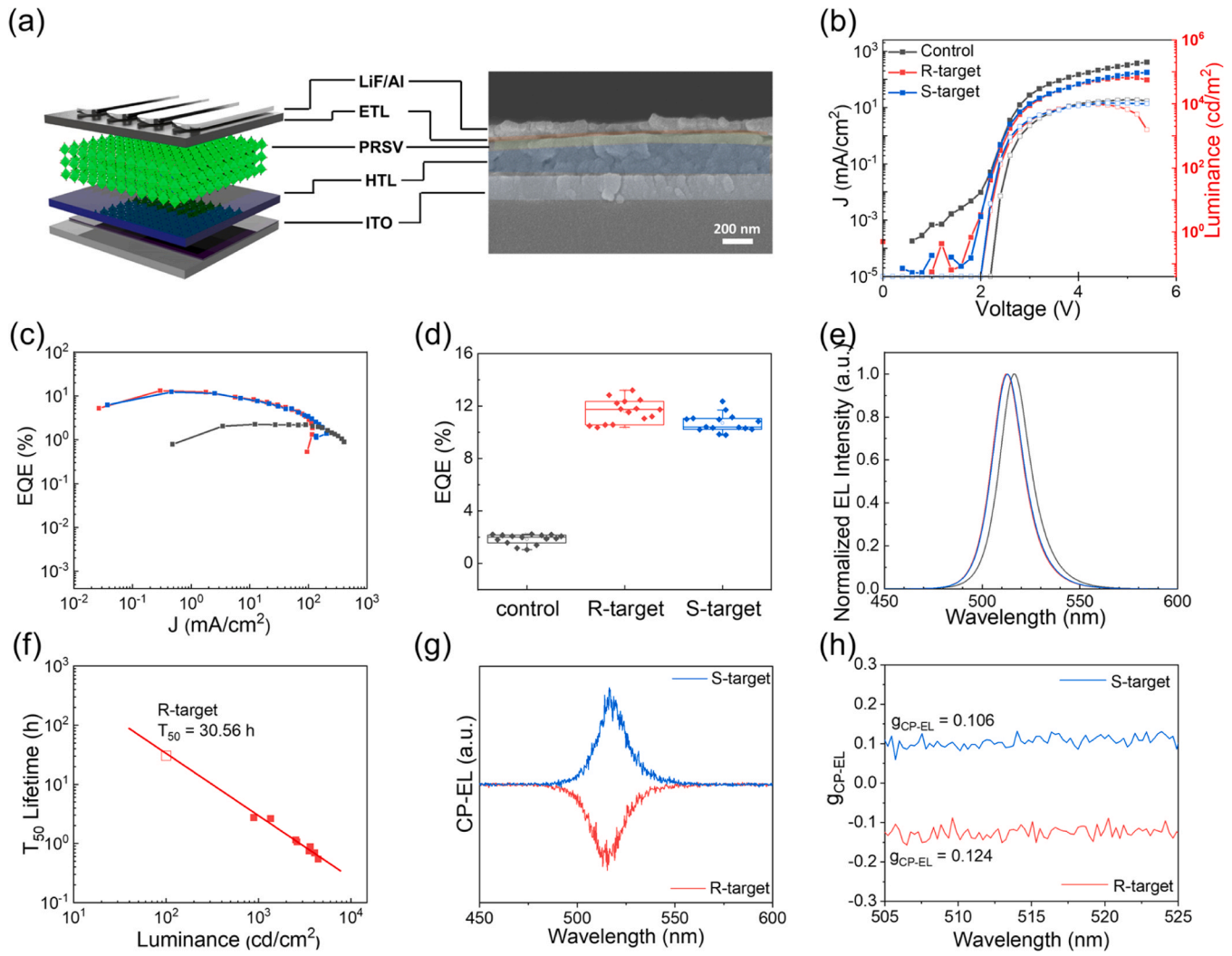

Fig. 4. Device structure and electroluminescence (EL) characteristics of Spin-LEDs. (a) Device structure and cross-sectional SEM image of the target spin-LEDs. (b) Current density–voltage–luminance curves. (c) External quantum efficiency (EQE)–current density curves. (d) Histogram of peak EQEs. (e) Normalized EL spectra of the control and R-/S- target spin-LEDs. (f) T_{50} lifetime-luminance curve obtained through accelerated lifetime test of the R-target spin-LEDs. (g) Difference between the L- and R-CP-EL intensities (I_{left}-I_{right}). (h) Dissymmetry factors ($g_{CP\text{-}EL}$) for the R-/S- target spin-LEDs.

recombined to form spin excitons, generating CP-EL. This rapid recombination was further promoted by the large exciton binding energy originating from strong carrier and dielectric confinement provided by the perovskite/BINAPO core–shell structure. Finally, the $g_{CP\text{-}EL}$ values of the R- and S-target perovskite devices were estimated to be −0.128 and 0.106, respectively (Fig. 4h and Fig. S25). These increased $g_{CP\text{-}EL}$ values in the target perovskite devices can be attributed to the strong CISS effects induced by the optimized thickness of the chiral R-/S-BINAPO and the formation of spin excitons owing to the large exciton binding energy.

To the best of our knowledge, this study presents first demonstration of circularly polarized EL from thermally evaporated perovskite spin-LEDs. The R- and S-target devices simultaneously achieve high EQE and high $g_{CP\text{-}EL}$ values, comparable to those of solution-processed perovskite perovskite spin-LEDs (Table S3).

4. Conclusion

In summary, we successfully fabricated thermally evaporated perovskite spin-LEDs by incorporating a well-defined perovskite/BINAPO core–shell structure. The chiral BINAPO shell imparted enhanced optoelectronic and chiro-optical properties to the target perovskite. In particular, the chiral BINAPO shell effectively regulated crystallization, leading to a significant reduction in the grain size of the perovskite. This core–shell structure enhanced the exciton binding energy through strong carrier and dielectric confinement at the organic–inorganic interface. Furthermore, the bidentate $(P=O)_2$ groups of the BINAPO shell were found to coordinate with the under-coordinated Pb^{2+} ions, suppressing trap-assisted non-radiative recombination and improving the optoelectronic properties. In terms of the chiro-optical functionality, the BINAPO shell acted as a CISS-active layer to control the spin states of the injected carriers. These carriers were subsequently transferred to the perovskite core to form spin excitons, which efficiently recombined to generate CP-EL. Consequently, our devices achieved a maximum EQE of 13.20% (R-target) and 12.35% (S-target), in conjunction with an EL dissymmetry factor of −0.124 (R-target) and 0.106 (S-target). These findings represent the first demonstration of CP-EL from thermally evaporated perovskite spin-LEDs, establishing a scalable platform for high-efficiency spin optoelectronics.

Authors contributions

(M.H.L. and Y.-J.C.) These authors contributed equally. M. H. Lee deposited perovskite film, fabricated the devices and characterized their

chemical, electrical and optical properties and wrote this paper. Y. -J. Choi measured CD-spectra, CPL spectra, and mCP-AFM and analyzed the results. J. Kim measured TEM and analyzed the results. D. Kim measured 2D GIWAXS experiment and analyzed the results. J. Han measured CP-EL for CP-LED. J. Kim measured TGA analysis. M. H. song supervised it. D.W.K. contributed equally to this work.

CRediT authorship contribution statement

Juyoung Kim: Investigation, Formal analysis. **Dongeun Kim:** Investigation, Formal analysis. **Donghan Kim:** Validation, Investigation, Formal analysis. **Jinkyu Yang:** Validation, Investigation, Formal analysis. **Jungho Han:** Validation, Investigation, Formal analysis. **Jongbeom Kim:** Validation, Investigation, Formal analysis. **Yong-Jun Choi:** Writing – original draft, Visualization, Validation, Investigation, Formal analysis, Data curation, Conceptualization. **Min Hyeong Lee:** Writing – original draft, Visualization, Validation, Methodology, Investigation, Formal analysis, Data curation, Conceptualization. **Myoung Hoon Song:** Writing – original draft, Visualization, Validation, Supervision, Resources, Project administration, Funding acquisition, Formal analysis, Data curation, Conceptualization. **Young Chul Jun:** Validation, Supervision, Project administration. **Han Gi Chae:** Supervision, Project administration.

Declaration of Competing Interest

The authors declare that they have no known competing financial interests or personal relationships that could have appeared to influence the work reported in this paper.

Acknowledgements

This work was supported by the National Research Foundation of Korea (NRF) grant funded by the Korea government (MSIT) (RS-2025–00514448 and RS-2025–25420303). This study contains the results obtained by using the equipment of UNIST Central Research Facilities (UCRF).

Appendix A. Supporting information

Supplementary data associated with this article can be found in the online version at doi:10.1016/j.nanoen.2026.111859.

Data availability

Data will be made available on request.

References

[1] L.N. Quan, F.P. García de Arquer, R.P. Sabatini, E.H. Sargent, Perovskites for Light emission, Adv. Mater. 30 (2018) 1801996, https://doi.org/10.1002/adma.201801996.
[2] H. Cho, S.-H. Jeong, M.-H. Park, Y.-H. Kim, C. Wolf, C.-L. Lee, J.H. Heo, A. Sadhanala, N. Myoung, S. Yoo, S.H. Im, R.H. Friend, T.-W. Lee, Overcoming the electroluminescence efficiency limitations of perovskite light-emitting diodes, Science 350 (2015) 1222–1225, https://doi.org/10.1126/science.aad1818.
[3] Z.-K. Tan, R.S. Moghaddam, M.L. Lai, P. Docampo, R. Higler, F. Deschler, M. Price, A. Sadhanala, L.M. Pazos, D. Credgington, F. Hanusch, T. Bein, H.J. Snaith, R. H. Friend, Bright light-emitting diodes based on organometal halide perovskite, Nat. Nanotechnol. 9 (2014) 687–692, https://doi.org/10.1038/nnano.2014.149.
[4] X.-K. Liu, W. Xu, S. Bai, Y. Jin, J. Wang, R.H. Friend, F. Gao, Metal halide perovskites for light-emitting diodes, Nat. Mater. 20 (2021) 10–21, https://doi.org/10.1038/s41563-020-0784-7.
[5] C. Wang, H. Fei, Y. Qiu, Y. Yang, Z. Wei, Y. Tian, Y. Chen, Y. Zhao, Photoinduced birefringence and reversible optical storage in liquid-crystalline azobenzene side-chain polymers, Appl. Phys. Lett. 74 (1999) 19–21, https://doi.org/10.1063/1.123138.
[6] C. Wagenknecht, C.-M. Li, A. Reingruber, X.-H. Bao, A. Goebel, Y.-A. Chen, Q. Zhang, K. Chen, J.-W. Pan, Experimental demonstration of a heralded entanglement source, Nat. Photon 4 (2010) 549–552, https://doi.org/10.1038/nphoton.2010.123.
[7] X. Zhang, Y. Liu, J. Han, Y. Kivshar, Q. Song, Chiral emission from resonant metasurfaces, Science 377 (2022) 1215–1218, https://doi.org/10.1126/science.abq7870.
[8] X. Zhan, F.F. Xu, Z. Zhou, Y. Yan, J. Yao, Y.S. Zhao, 3D laser displays based on circularly polarized lasing from cholesteric liquid crystal arrays, Adv. Mater. 33 (2021) 2104418, https://doi.org/10.1002/adma.202104418.
[9] G. Long, C. Jiang, R. Sabatini, Z. Yang, M. Wei, L.N. Quan, Q. Liang, A. Rasmita, M. Askerka, G. Walters, X. Gong, J. Xing, X. Wen, R. Quintero-Bermudez, H. Yuan, G. Xing, X.R. Wang, D. Song, O. Voznyy, M. Zhang, S. Hoogland, W. Gao, Q. Xiong, E.H. Sargent, Spin control in reduced-dimensional chiral perovskites, Nat. Photon 12 (2018) 528–533, https://doi.org/10.1038/s41566-018-0220-6.
[10] M.P. Hautzinger, X. Pan, S.C. Hayden, J.Y. Ye, Q. Jiang, M.J. Wilson, A.J. Phillips, Y. Dong, E.K. Raulerson, I.A. Leahy, C.-S. Jiang, J.L. Blackburn, J.M. Luther, Y. Lu, K. Jungjohann, Z.V. Vardeny, J.J. Berry, K. Alberi, M.C. Beard, Room-temperature spin injection across a chiral perovskite/III–V interface, Nature 631 (2024) 307–312, https://doi.org/10.1038/s41586-024-07560-4.
[11] Q. Wang, H. Zhu, Y. Tan, J. Hao, T. Ye, H. Tang, Z. Wang, J. Ma, J. Sun, T. Zhang, F. Zheng, W. Zhang, H.W. Choi, W.C.H. Choy, D. Wu, X.W. Sun, K. Wang, Spin quantum dot light-emitting diodes enabled by 2D chiral perovskite with spin-dependent carrier transport, Adv. Mater. 36 (2024) 2305604, https://doi.org/10.1002/adma.202305604.
[12] Y.-H. Kim, Y. Zhai, H. Lu, X. Pan, C. Xiao, E.A. Gaulding, S.P. Harvey, J.J. Berry, Z. V. Vardeny, J.M. Luther, M.C. Beard, Chiral-induced spin selectivity enables a room-temperature spin light-emitting diode, Science 371 (2021) 1129–1133, https://doi.org/10.1126/science.abf5291.
[13] Y.-J. Choi, H. Guo, J. Han, J. Han, M.H. Lee, W.-W. Park, D. Kim, J. Kim, J. Yang, D. Lee, D. Kim, O.-H. Kwon, Y.C. Jun, S.G. Lee, M.H. Song, Structural Distortion-Driven Chirality Transfer and Circularly Polarized Light Emission in Quasi-2D Perovskites Based Light-Emitting Diodes, Adv. Funct. Mater. n/a e25181. DOI: 10.1002/adfm.202525181.
[14] J. Yin, D. Zhao, Y. Qiao, J. Zhao, R. Jiang, P. Tian, W. Zhang, B. Wang, G. Xing, R. Guo, S. Mei, Bifunctional spacer cation enables high-efficiency chiral red quasi-2D perovskite light-emitting diodes via defect passivation and chirality enhancement, ACS Photon 13 (2026) 263–273, https://doi.org/10.1021/acsphotonics.5c02211.
[15] W. Wu, X. Shang, Z. Xu, H. Ye, Y. Yao, X. Chen, M. Hong, J. Luo, L. Li, Toward efficient two-photon circularly polarized light detection through cooperative strategies in chiral quasi-2D perovskites, Adv. Sci. 10 (2023) 2206070, https://doi.org/10.1002/advs.202206070.
[16] J. Yao, Z. Wang, Y. Huang, J. Xue, D. Zhang, J. Chen, X. Chen, S.-C. Dong, H. Lu, Efficient green spin light-emitting diodes enabled by ultrafast energy- and spin-funneling in chiral perovskites, J. Am. Chem. Soc. 146 (2024) 14157–14165, https://doi.org/10.1021/jacs.4c02821.
[17] B. Li, Y. Li, W. Yuan, X. Zhang, S. Tao, H. Zhan, Z.-g Yu, K. Wang, J. liu, L. Wang, C. Qin, Chiral Quasi-2D perovskites based single junction spin-light-emitting diodes, Adv. Funct. Mater. 35 (2025) 2415433, https://doi.org/10.1002/adfm.202415433.
[18] S. He, W. Lin, D. Yu, J. Shi, Z. Yin, C. Sun, H. Liu, C. Zhang, J. Yuan, S. Bai, S. Xiao, G. Long, M. Yuan, Y. Jiang, Y. Chen, Q. Song, Perovskite spin light-emitting diodes with simultaneously high electroluminescence dissymmetry and high external quantum efficiency, Nat. Commun. 16 (2025) 2201, https://doi.org/10.1038/s41467-025-57472-8.
[19] C.-H. Yang, H. Xiao, Y.-F. Sang, J. Luo, S.-B. Xiao, H.-L. Xuan, Q.-R. Ding, W. Lin, Z.-X. Xu, Z.-N. Chen, L.-J. Xu, Situ formed perovskite nanocrystal films toward efficient circularly polarized electroluminescence, Adv. Funct. Mater. 34 (2024) 2310500, https://doi.org/10.1002/adfm.202310500.
[20] G. Jang, D.-Y. Jo, S. Ma, J. Lee, J. Son, C.U. Lee, W. Jeong, S. Yang, J.H. Park, H. Yang, J. Moon, Core–shell perovskite quantum dots for highly selective room-temperature spin light-emitting diodes, Adv. Mater. 36 (2024) 2309335, https://doi.org/10.1002/adma.202309335.
[21] E.I. Jung, H.J. Lee, J. Kim, Q.T. Siddiqui, M. Kim, Z. Lin, C. Park, D.H. Kim, Recent progress on chiral perovskites as chiroptical active layers for next-generation LEDs, Mater. Sci. Eng. R. 160 (2024) 100817, https://doi.org/10.1016/j.mser.2024.100817.
[22] Y.-H. Kim, R. Song, J. Hao, Y. Zhai, L. Yan, T. Moot, A.F. Palmstrom, R. Brunecky, W. You, J.J. Berry, J.L. Blackburn, M.C. Beard, V. Blum, J.M. Luther, The structural origin of chiroptical properties in perovskite nanocrystals with chiral organic ligands, Adv. Funct. Mater. 32 (2022) 2200454, https://doi.org/10.1002/adfm.202200454.
[23] M.K. Jana, R. Song, H. Liu, D.R. Khanal, S.M. Janke, R. Zhao, C. Liu, Z.V. Vardeny, V. Blum, D.B. Mitzi, Organic-to-inorganic structural chirality transfer in a 2D hybrid perovskite and impact on Rashba–Dresselhaus Spin–Orbit Coupling, Nat. Commun. 11 (2020) 4699, https://doi.org/10.1038/s41467-020-18485-7.
[24] R. Song, R. Zhao, Density functional theory study of two-dimensional hybrid organic–inorganic perovskites: frontier level alignment and chirality-induced spin splitting, AAPPS Bull. 34 (2024) 20, https://doi.org/10.1007/s43673-024-00125-7.
[25] H. Lu, C. Xiao, R. Song, T. Li, A.E. Maughan, A. Levin, R. Brunecky, J.J. Berry, D. B. Mitzi, V. Blum, M.C. Beard, Highly distorted chiral two-dimensional tin iodide perovskites for spin polarized charge transport, J. Am. Chem. Soc. 142 (2020) 13030–13040, https://doi.org/10.1021/jacs.0c03899.
[26] C. Ye, J. Jiang, S. Zou, W. Mi, Y. Xiao, Core–shell three-dimensional perovskite nanocrystals with chiral-induced spin selectivity for room-temperature spin light-emitting diodes, J. Am. Chem. Soc. 144 (2022) 9707–9714, https://doi.org/10.1021/jacs.2c01214.

[27] J. Xu, K. Li, U.N. Huynh, M. Fadel, J. Huang, R. Sundararaman, V. Vardeny, Y. Ping, How spin relaxes and dephases in bulk halide perovskites, Nat. Commun. 15 (2024) 188, https://doi.org/10.1038/s41467-023-42835-w.
[28] J. Luo, J. Li, L. Grater, R. Guo, A.R.B. Mohd Yusoff, E. Sargent, J. Tang, Vapour-deposited perovskite light-emitting diodes, Nat. Rev. Mater. 9 (2024) 282–294, https://doi.org/10.1038/s41578-024-00651-8.
[29] J. Li, P. Du, Q. Guo, L. Sun, Z. Shen, J. Zhu, C. Dong, L. Wang, X. Zhang, L. Li, C. Yang, J. Pan, Z. Liu, B. Xia, Z. Xiao, J. Du, B. Song, J. Luo, J. Tang, Efficient all-thermally evaporated perovskite light-emitting diodes for active-matrix displays, Nat. Photon 17 (2023) 435–441, https://doi.org/10.1038/s41566-023-01177-1.
[30] M.H. Lee, J. Kim, J. Han, Y.I. Kim, D.H. Kim, Y.-J. Choi, M.H. Song, Fabrication of conductive perovskite-additive networks via sequential vacuum deposition for perovskite light-emitting diodes, ACS Energy Lett. 10 (2025) 2898–2905, https://doi.org/10.1021/acsenergylett.5c01014.
[31] J.S. Kim, J.-M. Heo, G.-S. Park, S.-J. Woo, C. Cho, H.J. Yun, D.-H. Kim, J. Park, S.-C. Lee, S.-H. Park, E. Yoon, N.C. Greenham, T.-W. Lee, Ultra-bright, efficient and stable perovskite light-emitting diodes, Nature 611 (2022) 688–694, https://doi.org/10.1038/s41586-022-05304-w.
[32] Y. Wang, L. Luo, Z. Wang, B. Tawiah, C. Liu, J.H. Xin, B. Fei, W.-Y. Wong, Growing Poly(norepinephrine) layer over individual nanoparticles to boost hybrid perovskite photocatalysts, ACS Appl. Mater. Inter 12 (2020) 27578–27586, https://doi.org/10.1021/acsami.0c06081.
[33] S. Zheng, Z. Wang, N. Jiang, H. Huang, X. Wu, D. Li, Q. Teng, J. Li, C. Li, J. Li, T. Pang, L. Zeng, R. Zhang, F. Huang, L. Lei, T. Wu, F. Yuan, D. Chen, Ultralow voltage–driven efficient and stable perovskite light-emitting diodes, Sci. Adv. 10 (2024) eadp8473, https://doi.org/10.1126/sciadv.adp8473.
[34] X. Yang, L. Ma, M. Yu, H.-H. Chen, Y. Ji, A. Hu, Q. Zhong, X. Jia, Y. Wang, Y. Zhang, R. Zhu, X. Wang, C. Lu, Focus on perovskite emitters in blue light-emitting diodes, Light. Sci. Appl. 12 (2023) 177, https://doi.org/10.1038/s41377-023-01206-2.
[35] C. Katan, N. Mercier, J. Even, Quantum and dielectric confinement effects in lower-dimensional hybrid perovskite semiconductors, Chem. Rev. 119 (2019) 3140–3192, https://doi.org/10.1021/acs.chemrev.8b00417.
[36] Y. Zhou, H. Li, T. Zhu, T. Gao, P. Yan, A highly luminescent chiral tetrahedral Eu4L4(L′)4 cage: chirality induction, chirality memory, and circularly polarized luminescence, J. Am. Chem. Soc. 141 (2019) 19634–19643, https://doi.org/10.1021/jacs.9b07178.
[37] D.-H. Kong, Y. Wu, C.-M. Shi, H. Zeng, L.-J. Xu, Z.-N. Chen, Highly efficient circularly polarized electroluminescence based on chiral manganese (ii) complexes, Chem. Sci. 15 (2024) 16698–16704, https://doi.org/10.1039/D4SC04748F.
[38] D. Liu, Y. Zhou, Y. Zhang, H. Li, P. Chen, W. Sun, T. Gao, P. Yan, Chiral BINAPO-controlled diastereoselective self-assembly and circularly polarized luminescence in triple-stranded europium(III) podates, Inorg. Chem. 57 (2018) 8332–8337, https://doi.org/10.1021/acs.inorgchem.8b00986.
[39] T. Harada, Y. Nakano, M. Fujiki, M. Naito, T. Kawai, Y. Hasegawa, Circularly Polarized Luminescence of Eu(III) complexes with point- and axis-chiral ligands dependent on coordination structures, Inorg. Chem. 48 (2009) 11242–11250, https://doi.org/10.1021/ic901663w.
[40] L. Xu, J. Li, B. Cai, J. Song, F. Zhang, T. Fang, H. Zeng, A bilateral interfacial passivation strategy promoting efficiency and stability of perovskite quantum dot light-emitting diodes, Nat. Commun. 11 (2020) 3902, https://doi.org/10.1038/s41467-020-17633-3.
[41] H. Xu, G. Xie, C. Han, Z. Zhang, Z. Deng, Y. Zhao, P. Yan, S. Liu, Influence of molecular configuration and functional substituents on excited state energy levels in two naphthyl-based phosphine oxide hosts, Org. Electron 13 (2012) 1516–1525, https://doi.org/10.1016/j.orgel.2012.05.003.
[42] Y. Shindo, Y. Ohmi, Problems of CD spectrometers. 3. Critical comments on liquid crystal induced circular dichroism, J. Am. Chem. Soc. 107 (1985) 91–97, https://doi.org/10.1021/ja00287a017.
[43] T. Narushima, H. Okamoto, Circular dichroism microscopy free from commingling linear dichroism via discretely modulated circular polarization, Sci. Rep. 6 (2016) 35731, https://doi.org/10.1038/srep35731.
[44] S.-H. Yang, R. Naaman, Y. Paltiel, S.S.P. Parkin, Chiral spintronics, Nat. Rev. Phys. 3 (2021) 328–343, https://doi.org/10.1038/s42254-021-00302-9.
[45] H. Lu, J. Wang, C. Xiao, X. Pan, X. Chen, R. Brunecky, J.J. Berry, K. Zhu, M. C. Beard, Z.V. Vardeny, Spin-dependent charge transport through 2D chiral hybrid lead-iodide perovskites, Sci. Adv. 5 (2019) eaay0571, https://doi.org/10.1126/sciadv.aay0571.
[46] I.C. Seo, S. Kim, B.H. Woo, I.-S. Chung, Y.C. Jun, Fourier-plane investigation of plasmonic bound states in the continuum and molecular emission coupling, Nanophotonics 9 (2020) 4565–4577, https://doi.org/10.1515/nanoph-2020-0343.